Quantum-Inspired Optimization for 2-bit Quantized Phase-Only Metasurfaces With Near-Field Multiobjective Control

Yutong Jiang, *Graduate Student Member, IEEE*, Zhe Zheng, Shuai S. A. Yuan, *Member, IEEE*, Hao Xue, Long Li, *Senior Member, IEEE*, and Wei E. I. Sha, *Senior Member, IEEE*

***Abstract*—This article presents a robust quantum-inspired optimization framework for designing 2-bit quantized phase-only metasurfaces capable of precise near-field multiobjective control. Addressing the limitations of conventional methods [e.g., phase gradient (PG), simulated annealing (SA), genetic algorithm (GA)] in navigating the complex, high-dimensional design space and handling competing objectives, we employ the discrete simulated bifurcation (dSB) algorithm. A key innovation is the effective mapping of the electromagnetic problem to a quadratic unconstrained binary optimization (QUBO) problem for 2-bit phases, extensible to higher order unconstrained binary optimization (HUBO) for multiobjective scenarios (e.g., with a penalty method). To tackle the inherent tradeoffs in multiobjective focusing, we propose two novel strategies: an adaptive weighting scheme for achieving arbitrary intensity ratios, and a penalty method for enforcing energy uniformity. Numerical results demonstrate dSB's superior performance in single-point focusing, achieving high efficiency and a clean focal spot compared to benchmark methods. For multipoint focusing, dSB consistently achieves higher total efficiency and produces qualitatively cleaner patterns with significantly less energy leakage and interfocal interference, even for complex asymmetric patterns (like Z-shape). The practical fidelity of our optimized designs was rigorously validated through comprehensive full-wave simulations using HFSS, which inherently account for intricate metasurface coupling effects and real-world electromagnetic interactions, thereby confirming the robustness of our algorithmic approach. Furthermore, scalability analysis confirms the algorithm's favorable polynomial complexity [$O(N_{\text{spins}}^{1.95} - N_{\text{spins}}^{2.08})$], making it highly efficient for large metasurface arrays. This work provides a versatile and reliable approach for designing advanced near-field metasurfaces with intricate, user-defined functionalities.**

***Index Terms*—Combinatorial optimization, near-field focusing, phase quantization, phase-only metasurfaces, quantum-inspired method.**

Received 24 July 2025; revised 17 September 2025; accepted 4 October 2025. Date of publication 27 October 2025; date of current version 11 December 2025. This work was supported in part by the Youth Fund of the National Natural Science Foundation of China under Grant 62401443, in part by the Postdoctoral Fellowship Program (Grade C) of China, Postdoctoral Science Foundation under Grant GZC20250387, and in part by the China Postdoctoral Science Foundation under Grant 2024M752522. This article is an expanded version from the 2025 IEEE MTT-S International Wireless Symposium [DOI: 10.1109/IWS65943.2025.11177845]. *(Corresponding author: Wei E. I. Sha.)*

Yutong Jiang, Shuai S. A. Yuan, and Wei E. I. Sha are with the College of Information Science and Electronic Engineering, Zhejiang University, Hangzhou 310027, China (e-mail: weisha@zju.edu.cn).

Zhe Zheng, Hao Xue, and Long Li are with the Key Laboratory of High-Speed Circuit Design and EMC, Ministry of Education, Xidian University, Xi'an 710071, China.

Digital Object Identifier 10.1109/TMTT.2025.3619563

I. Introduction

METASURFACES, artificially engineered 2-D metamaterials, have significantly advanced electromagnetic wave manipulation due to their exceptional ability to precisely control phase, amplitude, and polarization at subwavelength scales [1], [2], [3]. Among these capabilities, quantized phase-only arrays, achieved through the judicious design of subwavelength structures, are particularly attractive [4], [5], [6]. This approach not only simplifies control mechanisms by limiting the number of phase states, but also offers economic benefits in fabrication and integration, and enables highly efficient manipulation of electromagnetic waves, ultimately facilitating the development of compact, high-performance devices [7]. Consequently, these versatile platforms are widely applied across diverse fields, ranging from advanced optics and holography to efficient wireless communications and biomedical sensing [8], [9], [10]. While much early research focused on far-field phenomena, the near-field manipulation capabilities of metasurfaces have recently garnered substantial attention. This growing interest stems from their unique capacity to control evanescent waves and provide highly localized field enhancements, unlocking exciting possibilities beyond traditional far-field applications. Specifically, this area holds immense promise for high-resolution imaging, enabling super-resolution capabilities by overcoming the diffraction limit; nonradiative energy transfer, crucial for efficient wireless power transmission over short distances; advanced sensing, allowing for highly sensitive detection of subtle changes in local environments; and secure near-field communications, providing robust data transfer in close proximity [11], [12], [13], [14], [15], [16]. These burgeoning applications underscore the critical need for sophisticated methods that can effectively control and optimize near-field electromagnetic fields to achieve high-performance functionalities.

Despite the immense potential of near-field metasurfaces, achieving precise and efficient near-field focusing, particularly with quantized phase-only arrays preferred for their cost-efficiency and hardware simplicity, remains a significant challenge. Unlike far-field scenarios where wave propagation is relatively straightforward, near-field interactions involve complex evanescent waves and strong coupling effects, making the design and optimization highly intricate [17]. Existing design methodologies prove inadequate in addressing these complexities. Semianalytical approaches (e.g., phase gradient

TABLE I
COMPARISON OF PRESENT WORK WITH PREVIOUS STUDIES

Work	Optimization Target	Application Scenario	Array Size	Core Contribution
Prior Work A [38]	Far-field beamforming (single/ multi-beam with nulls)	Far-field communication	10×24	First application of a quantum-inspired algorithm to antenna arrays for far-field beamforming
Prior Work B [39]	Space-time coding metasurface (frequency domain control)	Space-time modulation, harmonic beamforming	20×20	First application of a quantum-inspired algorithm to **space-time coding** metasurface design
Prior Work C [40]	Single-point near-field focusing	Near-field mmWave communication	41×41	First application of the quantum-inspired algorithm to **single point near-field** focusing
Present Work	**Multi-objective near-field control** (multi-point focusing & power homogenization)	Near-field imaging, electromagnetic therapy, multi-task communication	41×41	First application of a quantum-inspired method to **multi-objective near-field control** with **adaptive weighting** and a **penalty method**

(PG) synthesis), while quick, are fundamentally constrained to simple scenarios due to their reliance on geometric optics approximations, and inherently suffer from sidelobe amplification in practical implementations caused by phase quantization errors [18], [19]. Stochastic optimization algorithms (e.g., genetic algorithms (GAs), simulated annealing (SA), particle swarm optimization) attempt to address nonconvexity through stochastic search mechanisms [20], [21], [22]. However, their prohibitive computational complexity and suboptimal convergence behavior often render them impractical for large array optimization. More recently, deep learning approaches aim to establish end-to-end mappings between electromagnetic signatures and beam parameters [23], [24]. Nevertheless, they suffer from critical data dependence; training requires exhaustive phase-field datasets whose acquisition incurs prohibitive experimental costs. Consequently, current approaches confront a fundamental trilemma—the mutually exclusive demands of solution optimality, optimization efficiency, and physical realizability. This highlights an urgent need for more efficient and robust optimization techniques capable of navigating the complex design landscape of near-field metasurfaces to achieve desired focusing performance.

To overcome these challenges, quantum and quantum-inspired algorithms have emerged as promising alternatives [25], [26], [27]. These algorithms draw inspiration from quantum mechanics principles like quantum superposition, entanglement, or tunneling, enabling them to explore vast solution spaces and escape local optima more effectively than traditional methods [28], [29], [30]. For instance, quantum annealing has shown remarkable success in optimizing complex combinatorial problems across various scientific and engineering disciplines [31], [32]. More recently, simulated bifurcation (SB) optimization, a novel quantum-inspired algorithm, has garnered significant attention for its ability to efficiently solve large-scale higher order unconstrained binary optimization (HUBO) problems [33], [34], [35]. This class of algorithms is particularly well-suited for electromagnetic design problems where the optimization landscape is often rugged, nonconvex, and fraught with numerous local minima [36], [37]. Their inherent ability to navigate complex energy landscapes makes them ideal candidates for the intricate design of metasurfaces, especially when aiming for highly specific and challenging near-field functionalities. Our group has successfully borrowed the quantum-inspired algorithm to solve complex electromagnetic design problems. Table I provides a comprehensive comparison of our previous and current work, clearly highlighting the unique contributions of this article [38], [39], [40].

Building on the promise of quantum-inspired optimization and addressing the limitations of existing methods, this article makes several significant contributions compared to our previous conference work [40].

1) First, this work presents a novel optimization framework that pioneers the application of a quantum-inspired algorithm to the intricate near-field focusing problem. We rigorously demonstrate its efficacy and superior performance through comprehensive numerical results and full-wave simulations.
2) Second, recognizing the inherent multiobjective nature of advanced near-field manipulation, we propose two distinct strategies for multiobjective optimization: a time-varying weight adjustment scheme and a novel objective function incorporating a penalty term. We thoroughly analyze the sensitivity of the multiobjective weights, providing a versatile and generalizable framework for achieving desired performance tradeoffs.
3) Finally, through extensive comparative studies, we conclude that a combination of analytical PG synthesis for single-point focusing and our proposed quantum-inspired optimization scheme for multiobjective Pareto front exploration offers an optimal balance between computational efficiency and superior focusing performance for near-field scenarios.

This work provides a robust and efficient approach for designing advanced phase-only quantized near-field metasurfaces.

The remainder of this article is organized as follows. Section II establishes the theoretical framework and formulates the near-field focusing problem, detailing metasurface unit-cell characteristics, near-field electromagnetic field calculation, and the mapping to a binary spin model through Hamiltonian formulation, including single-point focusing method and multipoints balancing strategies. Section III introduces the

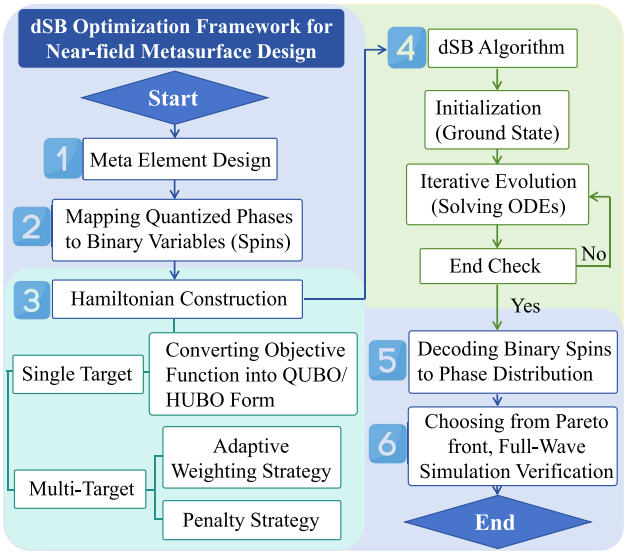

Fig. 1. Proposed quantum-inspired optimization framework for near-field metasurface design. The framework consists of six main parts, whose detailed workflow and functions are elaborated in Sections II–IV.

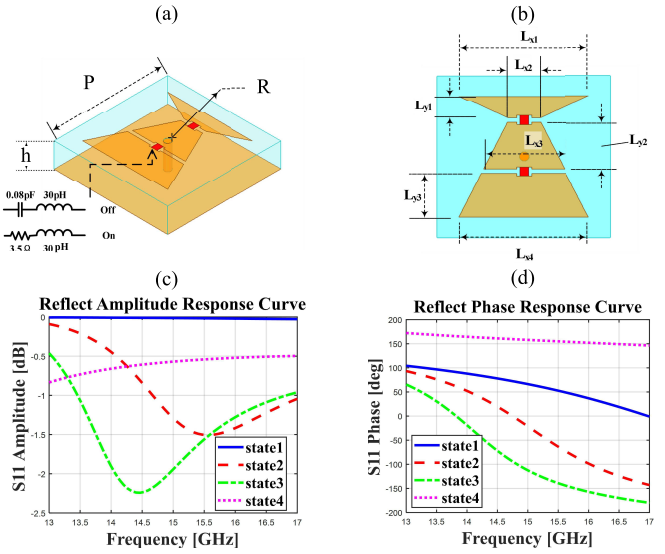

Fig. 2. Metasurface unit-cell design and performance characteristics. (a) Unit-cell structure with p-i-n diode and equivalent circuit model. (b) Geometric parameters of the fabricated unit-cell. (c) Reflection loss versus frequency for the four p-i-n diode states: State 1 ("−1, −1"), State 2 ("−1, +1"), State 3 ("+1, −1"), and State 4 ("+1, +1"). (d) Reflection phase versus frequency showing 2-bit quantization performance at 15 GHz.

quantum-inspired SB optimizer, discussing its various forms, underlying dynamics, and its performance evaluation. Comprehensive numerical results are presented and discussed in Section IV, which includes parameter setup and benchmarking of conventional methods, single-point focusing performance, detailed multipoint focusing scenarios (*yoz* and *xoy* plane targets), and an in-depth analysis of multiobjective tradeoffs and full-wave verification. Finally, Section V concludes this article by summarizing our key findings and outlining potential avenues for future research.

II. Theoretical Framework and Problem Formulation

This section details the theoretical framework of our proposed quantum-inspired optimization for near-field metasurface design. To provide a clear overview of the entire optimization procedure, we present the flowchart in Fig. 1. This figure summarizes the complete process from mapping the complex electromagnetic problem to a binary variable model, solving it with the discrete SB (dSB) algorithm, and finally verifying its performance. Sections II-A–II-D will discuss each step of the flowchart in detail.

A. Metasurface Phase Modulation and Spin Mapping

The designed metasurface unit-cell is illustrated in Fig. 2(a), where the electromagnetic simulation was conducted using the commercial software Ansys HFSS. Through the use of periodic boundary conditions in conjunction with Floquet ports, the simulation ensured accurate characterization of the reflection properties under infinite periodic array conditions. The red rectangular patch in Fig. 2(a) represents the p-i-n diode, specifically the SMP1320-040LF from SKYWORKS, along with its equivalent circuit model. The p-i-n diode exhibits distinct electrical characteristics in its two operational states: in the OFF state, it behaves as an *LC* circuit, while in the ON state, it functions as an *RL* circuit. The geometric parameters of the fabricated unit-cell are presented in Fig. 2(b), with the substrate having a relative permittivity of $\varepsilon_r = 2.65$ and a loss tangent of $\tan\delta = 0.001$. The detailed dimensions of the unit-cell are as follows: $L_{y1} = 0.95$ mm, $L_{y2} = 2.02$ mm, $L_{y3} = 1.88$ mm, $L_{x1} = 5.25$ mm, $L_{x2} = 1.34$ mm, $L_{x3} = 3.26$ mm, $L_{x4} = 5.25$ mm, $P = 7$ mm, $h = 1.5$ mm, and $R = 0.2$ mm.

The phase modulation characteristics of the metasurface unit-cell demonstrate excellent 2-bit quantization performance at 15 GHz, as shown in Fig. 2(d). The four distinct unit states are labeled in the figure legend as State 1 ("−1, −1"), State 2 ("−1, +1"), State 3 ("+1, −1"), and State 4 ("+1, +1"), exhibiting well-defined phase differences that conform to the ideal 2-bit reflection unit phase distribution. When both p-i-n_1 and p-i-n_2 are in the OFF state, representing the "−1, −1" unit configuration (State 1), the reflection phase is 66°. The "−1, +1" unit state (State 2), achieved with p-i-n_1 OFF and p-i-n_2 ON, yields a reflection phase of -21°. The "+1, −1" unit state (State 3), with p-i-n_1 ON and p-i-n_2 OFF, produces a reflection phase of -112°. Finally, when both p-i-n_1 and p-i-n_2 are in the ON state, representing the "+1, +1" unit configuration (State 4), the reflection phase reaches 158°. As illustrated in Fig. 2(c), the reflection loss remains within −2.3 dB across all four p-i-n diode states (State 1–State 4), indicating minimal power dissipation during phase modulation. These results demonstrate that the unit cell's reflection characteristics closely approximate those of an ideal 2-bit discrete phase modulator, making it suitable for advanced metasurface applications requiring precise phase control and efficient electromagnetic wave manipulation.

B. Near-Field Electromagnetic Field Calculation

To accurately design and optimize metasurfaces for near-field focusing, precisely calculating the electromagnetic field

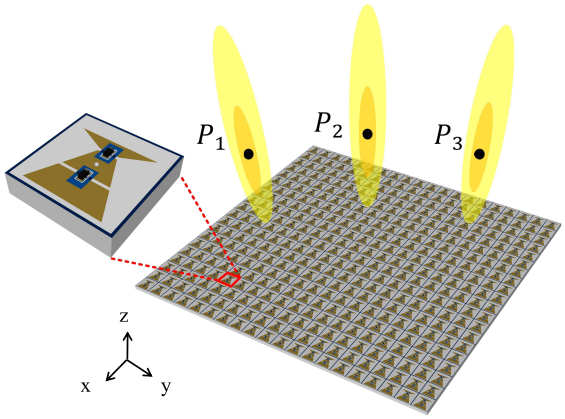

Fig. 3. Metasurface array design and near-field distribution optimization. The 20 × 20 metasurface array, composed of the designed unit cells, serves as an illustrative example. The three focal points P_1, P_2, and P_3 represent a typical near-field distribution pattern. The optimization algorithm determines the p-i-n diode states across the entire metasurface to generate the desired near-field distribution. All simulations are configured with the metasurface on the *xoy* plane, modulating *x*-polarized normally incident plane waves, ensuring full-wave simulation results closely approximate the near-field distribution calculated under quantized phase constraints for algorithm validation.

distribution in the proximity of the metasurface is essential. The metasurfaces are placed in the *xoy* plane as illustrated in Fig. 3. Unlike far-field scenarios, near-field interactions involve complex evanescent waves and strong coupling effects between the metasurface elements and the focal plane, necessitating a rigorous electromagnetic foundation.

The electromagnetic foundation of our methodology is established through the first-principles Maxwell formulation. Departing from conventional scalar potential approximations, we rigorously model the vector field interactions using dyadic Green's function formalism. The electric field distribution $\mathbf{E}(\mathbf{r})$ generated by an N-element metasurface array, modeled as a planar configuration of current sources (e.g., equivalent electric dipoles or surface currents) positioned in the *xoy* plane at $z = 0$ as illustrated in Fig. 3, can be expressed as [41]

$$\mathbf{E}(\mathbf{r}) = -j\omega\mu \sum_{n=1}^{N} \int \bar{\mathbf{G}}(\mathbf{r}, \mathbf{r}') \cdot \mathbf{J}_n(\mathbf{r}') d\mathbf{r}' \tag{1}$$

where $\mathbf{J}_n(\mathbf{r}')$ represents the equivalent current density of the nth metasurface element located at $\mathbf{r}'_n$, which is directly related to its complex transmission coefficient (amplitude and phase). ω is the angular frequency, and μ is the permeability of the medium. The term $\bar{\mathbf{G}}(\mathbf{r}, \mathbf{r}') \in \mathbb{C}^{3\times3}$ denotes the dyadic Green's function, which describes the vector propagation of the electromagnetic wave from a source point $\mathbf{r}'$ to an observation point $\mathbf{r}$. For free space, the dyadic Green's function can be expressed in terms of the unit dyad $\bar{\mathbf{I}}$ and the scalar Green's function $g(\mathbf{r}, \mathbf{r}')$ as [41]

$$\bar{\mathbf{G}}(\mathbf{r}, \mathbf{r}') = \left(\bar{\mathbf{I}} + \frac{\nabla\nabla}{k^2}\right) g(\mathbf{r}, \mathbf{r}') \tag{2}$$

where k is the free-space wavenumber ($k = \omega\sqrt{\mu\epsilon}$), and $g(\mathbf{r}, \mathbf{r}')$ is the scalar Green's function for free space, given by $g(\mathbf{r}, \mathbf{r}') = (e^{-jk|\mathbf{r}-\mathbf{r}'|})/(4\pi|\mathbf{r} - \mathbf{r}'|)$. This method allows for a precise calculation of the complex vector near-field distribution, fully accounting for the intricate electromagnetic interactions.

While it is theoretically possible to incorporate the exact $\mathbf{J}_n(\mathbf{r}')$, in this work, we assume independent unit responses. This assumption not only allows for highly efficient and scalable computation but also makes our algorithm extensible to large-scale problems. However, we acknowledge that in real-world applications, nonideal factors such as mutual coupling between units and the effects of the feed network are vital and must be considered. Therefore, our subsequent full-wave simulation work is indispensable for verifying the effectiveness of our method under realistic physical conditions.

C. Mapping Near-Field Focusing to a Binary Spin Model: Hamiltonian Formulation

The successful application of quantum-inspired optimization algorithms, such as the dSB optimizer used in this work, critically depends on effectively mapping the complex electromagnetic field problem into an equivalent binary spin model [42], [43], [44], [45]. This transformation allows us to leverage the powerful search capabilities of these algorithms to navigate the vast combinatorial space of possible metasurface designs by casting the problem as either a quadratic unconstrained binary optimization (QUBO) problem or a HUBO problem [46], [47]. For the 2-bit phase quantization explored in this article, the problem naturally maps to a QUBO formulation. It is worth noting that this framework is not limited to the specific 2-bit unit demonstrated here. As long as the complex response of a unit cell in its various states can be obtained through electromagnetic simulation or measurement, it can be directly incorporated into our framework. Similarly, our prior work has successfully extended this approach to 3-bit phase control, which corresponds to an HUBO problem, demonstrating the versatility of mapping and algorithm solving [38].

For a metasurface with b-bit discrete phase control, each phase variable $\phi_n \in \{2\pi k/2^b \mid k = 0, 1, \ldots, 2^b - 1\}$ is encoded through b spin variables $\{s_{n1}, \ldots, s_{nb}\} \in \{-1, +1\}^b$. The general phase encoding is achieved via the expansion

$$e^{j\phi_n} = \sum_{k=1}^{2^{b-1}} c_k \prod_{i\in\mathcal{I}_k} s_{ni} \tag{3}$$

where $\mathcal{I}_k$ indexes the spins involved in the kth interaction term. Unlike binary or integer representations that may require artificial one-hot constraints or $O(b)$ bits per phase shifter, our spin encoding leverages the intrinsic $\{-1, +1\}$ symmetry of spins, allowing b spins to naturally represent 2^b distinct phase states. Specifically, for the 2-bit encoding ($b = 2$) employed in this article, each metasurface element's phase is represented by two spins (s_{n1} and s_{n2}). This allows for $2^2 = 4$ distinct phase states. The complex phase expression for the nth element is given by

$$e^{j\phi_n} = c_1 s_{n1} + c_2 s_{n2} \tag{4}$$

where $c_1 = (1 + j)/2$ and $c_2 = (1 - j)/2$. In this 2-bit case, the product term $\prod_{i\in\mathcal{I}_k} s_{ni}$ in (3) is a single spin s_{ni}. For higher

bit quantizations, the encoding scheme is more complex and referred to in our previous work [38].

To formulate the problem, we define $\mathbf{J}_{n,\text{base}}(\mathbf{r}')$ as the fixed, unmodulated current density profile of the nth metasurface element, which inherently carries its magnitude and initial phase response (derived from full-wave simulations or measurements). The phase modulation is then applied by multiplying this base current profile by the spin-encoded phase factor. Thus, inserting the 2-bit phase encoding of $e^{j\phi_n}$ from (4) into the fundamental electric field expression (1) (from Section II-B), we obtain the spin-encoded field distribution $\mathbf{E}(\mathbf{r})$ at any observation point $\mathbf{r}$

$$\mathbf{E}(\mathbf{r}) = -j\omega\mu \sum_{n=1}^{N} (c_1 s_{n1} + c_2 s_{n2}) \int \bar{\mathbf{G}}(\mathbf{r}, \mathbf{r}') \cdot \mathbf{J}_{n,\text{base}}(\mathbf{r}') d\mathbf{r}' \quad (5)$$

where the integral term $\int \bar{\mathbf{G}}(\mathbf{r}, \mathbf{r}') \cdot \mathbf{J}_{n,\text{base}}(\mathbf{r}') d\mathbf{r}'$ represents the complex electric field contribution of the nth metasurface element to the observation point $\mathbf{r}$, specifically from its unmodulated base current profile. The term $(c_1 s_{n1} + c_2 s_{n2})$ then acts as a spin-dependent phase modulator for this contribution.

To optimize the metasurface for desired near-field focusing, we define a Hamiltonian $\mathcal{H}$ as an objective function whose minimization corresponds to achieving the target electromagnetic field distribution. This transforms the electromagnetic design problem into a combinatorial optimization task solvable by the dSB optimizer. For maximizing the field intensity at a target point $\mathbf{r}_0$, the Hamiltonian is defined as the negative squared magnitude of the electric field at that point

$$\mathcal{H} = -\mathbf{E}^*(\mathbf{r}_0) \cdot \mathbf{E}(\mathbf{r}_0). \quad (6)$$

Now, we substitute the spin-encoded field distribution from (5) into (6). For conciseness, we define the complex field contribution of the nth element (originating from its base current profile $\mathbf{J}_{n,\text{base}}(\mathbf{r}')$ and propagated by the dyadic Green's function) to the observation point $\mathbf{r}_0$ as

$$\mathbf{A}_n(\mathbf{r}_0) = -j\omega\mu \int \bar{\mathbf{G}}(\mathbf{r}_0, \mathbf{r}') \cdot \mathbf{J}_{n,\text{base}}(\mathbf{r}') d\mathbf{r}'. \quad (7)$$

Then, the spin-encoded field at $\mathbf{r}_0$ is

$$\mathbf{E}(\mathbf{r}_0) = \sum_{n=1}^{N} (c_1 s_{n1} + c_2 s_{n2}) \mathbf{A}_n(\mathbf{r}_0). \quad (8)$$

Substituting this into (6), the Hamiltonian becomes

$$\begin{aligned} \mathcal{H} &= -\left(\sum_{n=1}^{N} (c_1 s_{n1} + c_2 s_{n2}) \mathbf{A}_n(\mathbf{r}_0) \right)^* \\ &\quad \cdot \left(\sum_{m=1}^{N} (c_1 s_{m1} + c_2 s_{m2}) \mathbf{A}_m(\mathbf{r}_0) \right) \\ &= \sum_{n=1}^{N} \sum_{m=1}^{N} Q_{nm} (c_1^* s_{n1} + c_2^* s_{n2})(c_1 s_{m1} + c_2 s_{m2}) \end{aligned} \quad (9)$$

where the coupling coefficient Q_{nm} is defined as

$$Q_{nm} = -\left(\mathbf{A}_n^*(\mathbf{r}_0) \cdot \mathbf{A}_m(\mathbf{r}_0) \right). \quad (10)$$

This expanded form of the Hamiltonian directly reveals its dependence on the binary spin variables. For the 2-bit encoding used in this study, as shown in (4), the Hamiltonian in (9) explicitly represents a QUBO problem.

For multiobjective optimization with K target points (e.g., energy distribution across several points), we generalize the Hamiltonian as a weighted sum of individual objectives

$$\mathcal{H} = \sum_{k=1}^{K} w_k \left(-\mathbf{E}^*(\mathbf{r}_k) \cdot \mathbf{E}(\mathbf{r}_k) \right). \quad (11)$$

By substituting the spin-encoded field for each target point $\mathbf{r}_k$, and following a similar expansion as for the single-point case, this multiobjective Hamiltonian also takes a QUBO form for 2-bit systems. The total coupling coefficient matrix would then be a weighted sum of individual coupling coefficient matrices.

D. Multiobjective Optimization Strategies

Optimizing for a single focal point is a fundamental capability, and many advanced near-field applications demand the simultaneous satisfaction of multiple, often conflicting, objectives. For instance, designing for multiple focal points might lead to uneven energy distribution among them. A critical challenge arises because traditional single-objective approaches, which often sum individual performance metrics into a single Hamiltonian, can lead to degenerate solutions. Physically distinct metasurface configurations yield similar overall Hamiltonian values, but result in vastly different and often undesirable near-field distributions. This phenomenon, where the optimization successfully minimizes the numerical objective but fails to capture the desired physical outcome, is a form of energy degeneracy and is illustrated in Fig. 4, showing various near-field patterns that share a comparable Hamiltonian value. To address these complex design challenges and effectively explore the Pareto front of optimal solutions, we propose two distinct multiobjective optimization strategies tailored for near-field metasurface design: an adaptive weighting strategy that dynamically balances competing objectives, and a new objective function incorporating a penalty term to enforce specific design constraints or performance targets.

1) Adaptive Weighting Strategy: Our first strategy employs an adaptive weighting strategy to dynamically adjust the influence of individual objectives throughout the optimization process. This method enables the framework to converge toward arbitrary predefined intensity ratios across multiple focal points, offering significant flexibility in shaping complex energy distributions beyond uniform goals. This contrasts with static weighting in the original dSB framework, which struggles to guide the optimization toward specific target proportions.

At predetermined intervals Δt during the optimization, we evaluate the intensity, $I_k(t) = -H_k(t)$, for each of the K individual target points. For each point k, we utilize a set of predefined target intensity ratios $\{R_1, \ldots, R_K\}$. This adaptive scheme adjusts the weight $w_k(t + \Delta t)$ so that the achieved intensity $I_k(t)$ becomes proportional to its respective target ratio R_k. Objectives that are currently underperforming relative to their target ratio (i.e., the ratio $I_k(t)/R_k$ is lower than average

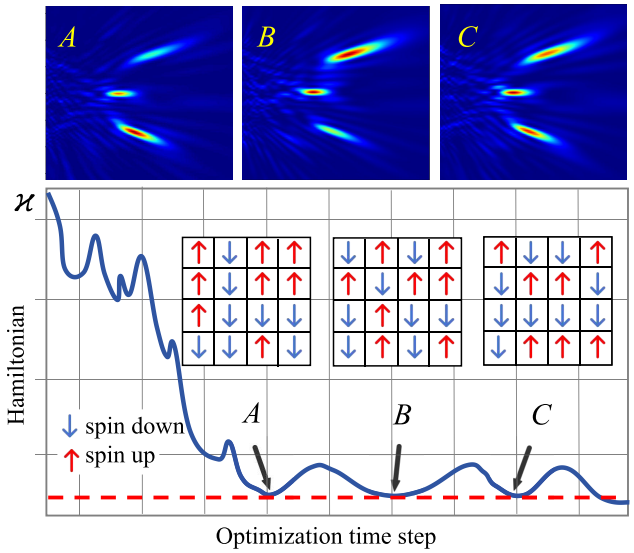

Fig. 4. A three-point focusing scenario where the Hamiltonian is defined as the sum of target point energies. With the evolution of the total Hamiltonian during optimization, it decreases as the number of optimization steps increases, with points A, B, and C marked. A, B, and C illustrate three distinct spin configurations corresponding to different phase profiles, where the arrows indicate spin up or spin down. While states A, B, and C all achieve the same minimum Hamiltonian, their corresponding near-field intensity distributions are significantly different. Configurations A and B result in nonuniform energy distribution, whereas C yields the desired uniform energy distribution across the target points.

across all points) will receive an increased weight, prioritizing their improvement.

The weight update mechanism proceeds as follows. The new weight for each objective is directly proportional to its target ratio and inversely proportional to its current achieved intensity. This ensures that objectives whose current intensity is significantly below their desired proportion will receive proportionally higher weights, thereby focusing the optimization effort where it is most needed

$$w_k(t+\Delta t) \propto \frac{R_k}{I_k(t)+\epsilon} \tag{12}$$

where ϵ is a small positive constant (e.g., 10^{-10}) added to the denominator to prevent division by zero, especially during early optimization steps when intensities might be very low. After calculating these raw proportional weights, they are then collectively normalized to maintain a constant sum (e.g., $\sum_{k=1}^{K} w_k(t+\Delta t) = K$), preventing the overall Hamiltonian magnitude from diverging. This iterative adjustment allows the algorithm to focus computational effort on the objectives that are most deficient relative to their individual target ratios, promoting a balanced and robust overall solution tailored to the desired arbitrary energy distribution. The choice of the update interval (number of steps) Δt is critical: an interval that is too short can introduce noisy fluctuations and prevent stable convergence, while an interval that is too long might delay rebalancing until the optimization is already close to local convergence, reducing the scheme's effectiveness.

While the concept of dynamically adjusting weights is widely used in multiobjective optimization, the novelty of our methodology lies in its creative and deep integration with the specific characteristics of the dSB algorithm. First, each of our weighting parameters is deeply bound to a specific physical objective (e.g., focusing uniformity, power efficiency). This provides valuable physical insight and allows our optimization to act as a direct control of physical phenomena, rather than a purely abstract mathematical calculation. Second, our strategy introduces a dynamically adjusted potential field, which constitutes a fundamental innovation at the physical layer of the SB algorithm. While standard SB theory is built on a fixed potential field, our strategy dynamically adjusts the objective function's weights after a specific number of evolution steps based on the current solution, and then continues the evolution in this new potential field. This dynamic approach utilizes the algorithm's "memory" from the evolution process and uses it as a basis for a more refined search in a promising region, effectively pioneering the algorithm in a dynamic optimization mode to solve complex electromagnetic problems.

2) Penalty Strategy: Our second multiobjective strategy employs a penalty method to directly enforce desired relationships among the intensities of multiple focal points. While the adaptive weighting scheme (Section II-D1) dynamically adjusts the influence of objectives, the penalty method directly modifies the Hamiltonian by adding a regularization term that penalizes deviations from the desired energy balance. This approach is particularly useful for achieving a more uniform energy distribution among multiple focal points or ensuring that specific energy differences are minimized.

For a set of K target points, the Hamiltonian is augmented with a penalty term that minimizes the squared differences in energy between all pairs of points. The objective function is modified as

$$\mathcal{H}_{\text{total}}(t) = \mathcal{H}_{\text{focus}} + \lambda(t) \sum_{i=1}^{K} \sum_{j=i+1}^{K} (I_i(\mathbf{r}) - I_j(\mathbf{r}))^2 \tag{13}$$

where $\mathcal{H}_{\text{focus}}$ is the primary focusing Hamiltonian, $I_i(\mathbf{r})$ and $I_j(\mathbf{r})$ represent the intensity at the target points i and j, respectively, and $\lambda(t)$ is a positive, time-dependent penalty scaling coefficient. To implement this penalty effectively, we adopt a dynamic constraint adjustment strategy for the penalty coefficient $\lambda(t)$. We treat $\lambda(t)$ as a dynamic parameter that gradually increases as the optimization progresses. This approach, often referred to as "softening" the constraints, allows the optimization process to explore a broader solution space in the early stages, where $\lambda(t)$ is small and the penalty is lenient. As iterations proceed and the system's "temperature" (borrowed from the SA context) decreases, $\lambda(t)$ is progressively increased. This guides the solution more strongly toward satisfying the energy balance constraint, ensuring that the system converges to a state that both achieves good overall focusing and adheres to the desired energy distribution. This dynamic scaling of $\lambda(t)$ is analogous to the temperature decay strategy in annealing algorithms, where a high temperature allows for greater exploration and less stringent adherence to constraints, while a low temperature enforces stricter compliance. Physically, this penalty term directly minimizes the squared difference in energy between every pair of target points, thereby encouraging a more equal energy distribution among them.

Crucially, since each intensity term $I_k(\mathbf{r})$ is inherently a quadratic function of the spin variables (as established in Section II-C), the squared difference $(I_i(\mathbf{r}) - I_j(\mathbf{r}))^2$ introduces up to fourth-order interactions among the spins. Consequently, incorporating this penalty term transforms the overall optimization problem into an HUBO problem.

III. Quantum-Inspired Optimization Algorithm

A. SB Optimizer

The SB optimizer, first proposed by Goto [33], is a powerful algorithm designed for efficiently solving large-scale combinatorial optimization problems, including QUBO and HUBO problems. Conceptually, SB simulates the adiabatic evolution of a system of coupled nonlinear oscillators, where the ground state of the oscillator system corresponds to the optimal binary solution (spin states of +1 or −1) of the target optimization problem.

As the applications of the SB algorithm have expanded, various forms have emerged, each tailored to different computational aspects or problem types [29]. The original continuous SB (cSB) formulation typically involves the time evolution of continuous oscillator amplitudes, where discrete binary solutions are obtained through a binarization step at the culmination of the simulation. In contrast, dSB, often referred to as binary SB (bSB), directly evolves or enforces discrete spin states (+1 or −1) throughout the optimization process. This characteristic makes dSB/bSB particularly well-suited for inherently binary optimization problems, as it bypasses the need for a separate post-binarization step. Furthermore, while all SB algorithms draw their conceptual roots from quantum mechanics, the term quantum SB (qSB) is sometimes used to denote formulations that maintain a closer fidelity to the underlying quantum mechanical framework or are specifically designed for potential execution on quantum hardware. In this work, we employ the dSB optimizer for its direct applicability to our discrete phase control problem, ensuring the solution remains in the binary spin space throughout optimization.

The core of the dSB optimizer lies in a classical-mechanical Hamiltonian that governs the time evolution of the oscillator system. Crucially, the Hamiltonian of our metasurface optimization problem, $\mathcal{H}$ (derived in Sections II-C and II-D), is embedded directly into this dSB framework as the objective function. This allows the dSB algorithm to leverage its internal dynamics to minimize $\mathcal{H}$, thereby finding the optimal metasurface phase configuration. The time evolution of the oscillator variables (representing the continuous amplitudes x_i and y_i of each oscillator, whose final signs determine the spins) is described by a set of ordinary differential equations (ODEs), derived from the system's Hamiltonian

$$\dot{x}_i = \Delta y_i, \tag{14}$$

$$\dot{y}_i = -\left[K x_i^2 - p(t) + \Delta\right] x_i - \frac{\xi_0}{2}\frac{\partial \mathcal{H}}{\partial x_i}. \tag{15}$$

These ODEs represent the classical approximation of the underlying quantum system's dynamics and form the fundamental basis for both cSB and dSB/bSB variants. Here, Δ represents the detuning frequency, K is the Kerr coefficient, and $p(t)$ is a time-dependent parametric pumping strength that gradually increases. All oscillator variables $\mathbf{x}$ and $\mathbf{y}$ are initialized around zero. As $p(t)$ progressively increases, each oscillator undergoes a bifurcation and transitions into a coherent state, where the final sign of x_i determines the corresponding spin variable's state (+1 or −1). These final spin states directly decode into the optimized phase configuration of the metasurface.

In our specific implementation of the dSB optimizer, we incorporate an explicit discrete enforcement mechanism: Once an oscillator's variable x_i reaches a threshold indicating convergence to either +1 or −1 (e.g., $|x_i| \geq 0.9$), its state is "locked" to that binary value for the remainder of the optimization process. This ensures that the evolving solution explicitly adheres to the binary spin constraint. Our dSB framework employs a dual-criteria approach for convergence. The primary termination condition is based on the locking of all spin variables, indicating that a stable solution has been found. The predefined maximum number of optimization steps serves as a secondary, safeguard mechanism to prevent the process from running indefinitely in highly complex scenarios.

The core of the dSB algorithm lies in the iterative solution of a pair of ODEs. The main computational cost in each iteration comes from calculating the full gradient vector. When the iteration step is fixed as set in our numerical results in Section IV, the theoretical computational complexity is always $O(N^2)$ for the 2-bit unit, where N is the number of metasurface cells. Specifically, in the single-point focusing scenario, the Hamiltonian $\mathcal{H}$ takes the form of a standard QUBO problem, as shown in (9). For a single spin variable, such as s_{n1}, the derivative is given by

$$\frac{\partial \mathcal{H}}{\partial s_{n1}} = \sum_{m=1}^{2N} Q_{n1,m} s_m. \tag{16}$$

Since this summation involves $2N$ terms and must be performed for each of the $2N$ spin variables, the total number of operations scales with N^2. For multipoint focusing with K target points using the adaptive weighting strategy, the total Hamiltonian is a weighted sum of the Hamiltonians for each point, as in (11). In each dSB iteration, the gradient of the total Hamiltonian is computed as

$$\nabla \mathcal{H}_{\text{total}} = \sum_{k=1}^{K} w_k \nabla \mathcal{H}_k. \tag{17}$$

Since each individual gradient $\nabla \mathcal{H}_k$ has a complexity of $O(N^2)$, the computational complexity for multipoint focusing is also $O(N^2)$. Furthermore, when using the penalty strategy for energy uniformity, the total Hamiltonian includes a fourth-order term. We compute its derivative with respect to each spin variable using the chain rule. The gradient of the penalty term

$$\mathcal{H}_{\text{penalty}} = \lambda(t) \sum_{i,j}^{K} (|E_i|^2 - |E_j|^2)^2 \tag{18}$$

is given by

$$\frac{\partial \mathcal{H}_{\text{penalty}}}{\partial s_k} = 2\lambda(t) \sum_{i,j}^{K} (|E_i|^2 - |E_j|^2) \left(\frac{\partial |E_i|^2}{\partial s_k} - \frac{\partial |E_j|^2}{\partial s_k} \right). \tag{19}$$

The derivative of the quadratic terms, $\partial|E|^2/\partial s_k$, is a linear function of the spin variables, and its calculation complexity is $O(N)$. When we scale this up to find the gradient for all $2N$ spin variables, the total complexity remains at the $O(N^2)$ level.

A significant advantage of the SB algorithm family (including dSB), particularly relevant for complex electromagnetic design, is its inherent capability to directly handle HUBO problems. While our current study's 2-bit phase encoding results in a QUBO problem, higher precision encodings (e.g., 3- or 4-bit) and a 2-bit penalty strategy for multiobjective optimization naturally lead to HUBO formulations. Unlike many quantum annealing approaches that often necessitate introducing auxiliary variables to reduce higher order terms to quadratic ones [48], [49], [50], which may exceed the qubit capacity of current quantum hardware, the SB algorithm directly processes these higher order interactions within its ODE-solving framework running on a classical computer [51]. This unique feature streamlines the optimization process for problems with complex, high-order spin correlations. Furthermore, the SB optimizer inherently supports massive parallel processing due to its simultaneous updating mechanism [34], making it a highly efficient solution for large-scale optimization tasks.

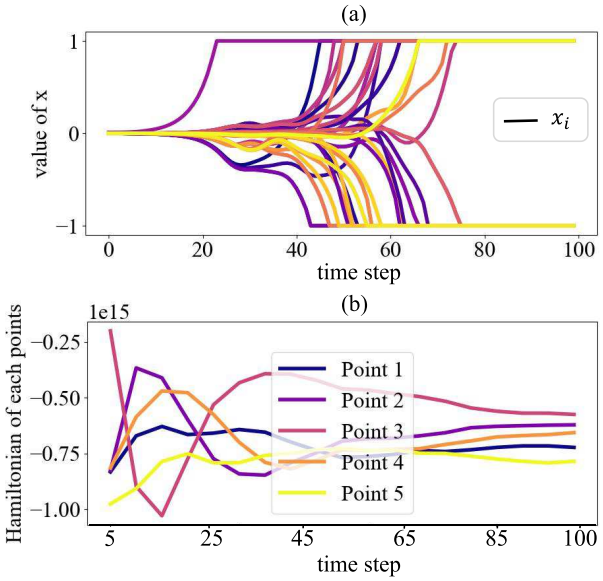

Fig. 5. Algorithm convergence and multiobjective dynamics. The horizontal axis represents the discrete time steps of the algorithm. (a) Evolution of Representative Oscillator Variables (x_i) and Spin Fixing: This figure illustrates the time evolution of the x_i values for a few representative oscillators during a SB optimization run for a five-point focusing scenario. (b) Evolution of Individual Objective Hamiltonians in Multi-Point Focusing: This figure shows the evolution of the Hamiltonian values for each of the five target points in a multi-point focusing scenario. Different curves represent individual objectives.

B. Performance Evaluation

1) Algorithm Dynamics and Convergence: In the optimization process, the continuous oscillator variables (x_i) evolve, eventually settling into binary states, which are then decoded to obtain the discrete phase values for the metasurface elements. We utilize a five-point focusing scenario as a case study to demonstrate the evolution of both individual spins and the Hamiltonians, employing our multiobjective strategies.

In a typical SB optimization run, the values of individual oscillator variables x_i initially fluctuate as the system explores the energy landscape. Fig. 5(a) visualizes this dynamic evolution, showcasing how representative x_i values for individual spins transition and stabilize in their final binary states over optimization steps. This demonstrates the algorithm's capability to effectively navigate from a continuous search space to a discrete solution. In this specific example, we observe that all spins reach their binary ± 1 states after approximately 80 steps, indicating that the algorithm has effectively converged to a stable and optimized solution.

For multipoint focusing problems, it is crucial to monitor how individual objectives evolve under our proposed strategies. Specifically, for the five-point beam focusing scenario, we track the Hamiltonian of each of the five target points (as relevant subcomponents of the total Hamiltonian) as a function of time step (sampling every five optimization steps). This allows us to observe how the adaptive weighting scheme dynamically balances performance among competing objectives. Fig. 5(b) illustrates this multiobjective convergence behavior, showing the evolution of the individual Hamiltonian components and providing insights into their respective balancing mechanisms. In this particular example, we observe that an initially large discrepancy between the maximum and minimum energy points is significantly reduced, leading to a much more uniform final energy distribution.

2) Weight Sensitivity Analysis: The precise selection of weighting coefficients is paramount in multiobjective optimization, as it directly influences the final performance tradeoffs and the balance among competing objectives. We conducted a comprehensive weight sensitivity analysis for our five-point focusing problem by systematically exploring $6^5 = 7776$ unique weight combinations, where each weight w_k for the kth target point varied from 1.0 to 2.0 with a step interval of 0.2. This exhaustive exploration allows us to thoroughly understand the impact of these weights on the achieved near-field focusing performance and to evaluate the robustness of our proposed multiobjective strategies. The key insights from this analysis are presented in Fig. 6.

Fig. 6 provides critical insights into the complex interplay between weighting coefficients and multiobjective performance. Fig. 6(a) illustrates the variation of overall uniformity by changing w_4 and w_5, while fixing w_1, w_2, and w_3 at 1.0. This heatmap demonstrates the sensitivity of uniformity to these specific weight combinations. We observe that even with optimized weights, the best achieved uniformity is approximately 0.575, indicating that achieving perfect uniform energy distribution is challenging for complex objectives. The distribution pattern reveals that optimal uniformity is typically achieved when the ratio of w_5/w_4 is approximately between 1.3 and 1.5.

Fig. 6(b) plots the results across all 6^5 weight combinations in a multidimensional performance space, specifically showing the tradeoff between total focusing energy and uniformity. This scatter plot reveals the performance boundary and the achievable Pareto front. It is evident that higher total focusing

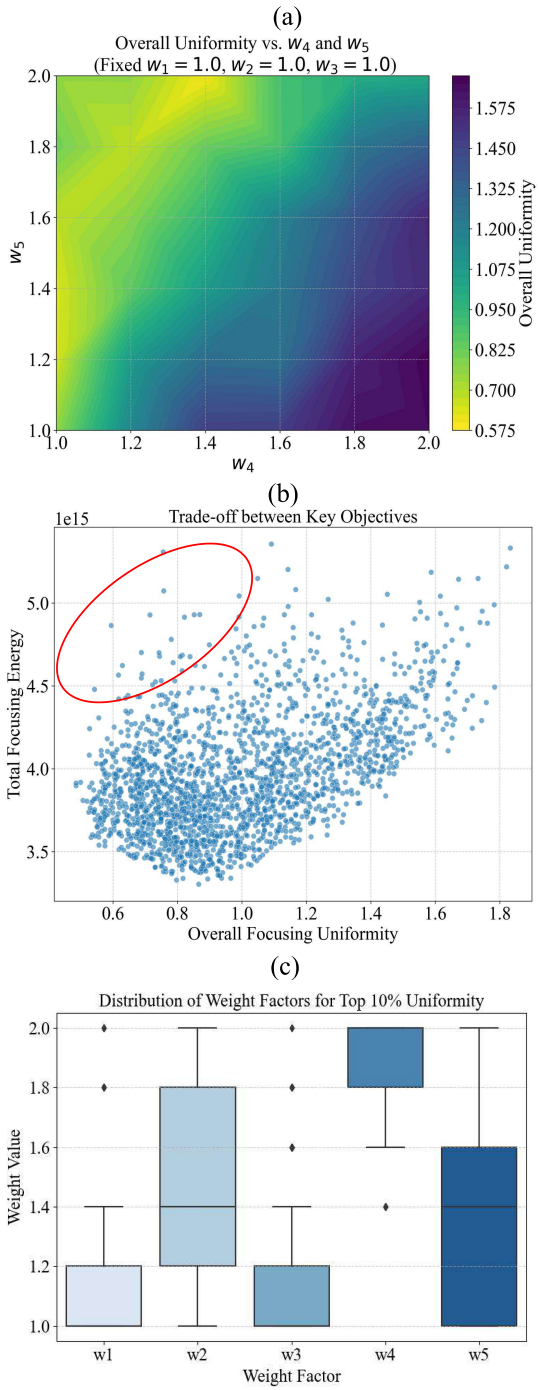

Fig. 6. Weight sensitivity analysis for multipoint near-field focusing. This figure illustrates the complex relationship between weighting coefficients and achieved performance in a five-point focusing scenario. (a) Uniformity as a function of w_4 and w_5. This heatmap visualizes the overall uniformity of focal intensities, with w_1, w_2, and w_3 fixed at 1.0. (b) Tradeoff between total focusing energy and uniformity for all weight combinations. This scatter plot reveals the achievable performance space, highlighting the Pareto front (marked by red circles) representing optimal compromises between maximizing total energy and achieving high uniformity. (c) Boxplot illustrating the distribution of weights for the top 10% uniformity results. The box represents the middle 50% of the data, with the median marked by the line inside. The lines extending from the box show the typical range of the data. Individual dots outside the box represent outliers that are significantly different from the rest of the set.

energy often comes at the expense of uniformity. The scatter points on the Pareto front, highlighted by red circles, represent a minority of the solutions that simultaneously achieve highly concentrated energy and relatively high uniformity. These solutions represent the most desirable compromises, and the final design selection would typically be made from this Pareto front.

Fig. 6(c) presents a boxplot analysis on the distribution of weighting factors (w_1–w_5) for the top 10% uniformity of results in the explored parameter space. The figure clearly demonstrates that w_1, w_3, and w_4 are relatively concentrated, indicating these parameters play a vital role in achieving high uniformity in this case. Furthermore, the presence of a few outliers (the black dots) in the distributions of w_1, w_3, and w_4 suggests that there are rare parameter combinations that can still yield excellent uniformity despite not conforming to the main pattern. This observation highlights the complexity of the optimization problem, as the optimal parameter region is difficult to find within the vast parameter space. And a simple two-weight sensitivity analysis, as shown in Fig. 6(a), is insufficient.

These analyses collectively indicate that the relationship between weighting coefficients and achieved multiobjective performance is highly sensitive and complex, making it challenging to identify optimal patterns through simple grid searches. This reinforces the competitive nature of resource allocation in multiobjective optimization and validates that our proposed multipoint optimization strategies are essential for effectively guiding the optimization direction. Relying solely on extensive grid search or conventional bisection methods would result in significant waste of time and computational resources for such intricate problems.

3) Scalability Analysis: To further evaluate the computational efficiency and practical applicability of the proposed dSB method, we thoroughly analyze its scalability by examining the relationship between the problem size and the required optimization time. In this case, the problem size is rigorously quantified by the total number of binary spins (N_{spins}), which is directly determined by the total number of metasurface elements (N_{elements}) and the phase bit resolution (n_{bits}), i.e., $N_{\text{spins}} = N_{\text{elements}} \times n_{\text{bits}}$. We performed this scalability analysis for three distinct near-field focusing scenarios: single-point focusing, multipoint focusing with the adaptive weighting scheme, and multipoint focusing using the penalty method, fixing the maximum iteration step as 5.

Fig. 7(a) illustrates the raw optimization time (in seconds) as a function of the total spin number (N_{spins}) on a linear scale. It clearly shows a nonlinear increase in computation time as the problem size grows for all three scenarios. We observe that single-point focusing requires the least computational time, followed by multipoint focusing with the adaptive weighting scheme. The penalty method generally demands the highest computational time, indicating the increased complexity associated with explicitly minimizing interpoint energy differences and the higher order objective Hamiltonian we use.

To more rigorously quantify the scalability, the same data is presented on a log-log scale in Fig. 7(b). This log-log plot allows for the estimation of the empirical computational complexity by fitting a power-law model ($T \propto N_{\text{spins}}^{\alpha}$) for each scenario. The resulting fits indicate polynomial growth in complexity across all methods: single-point focusing exhibits

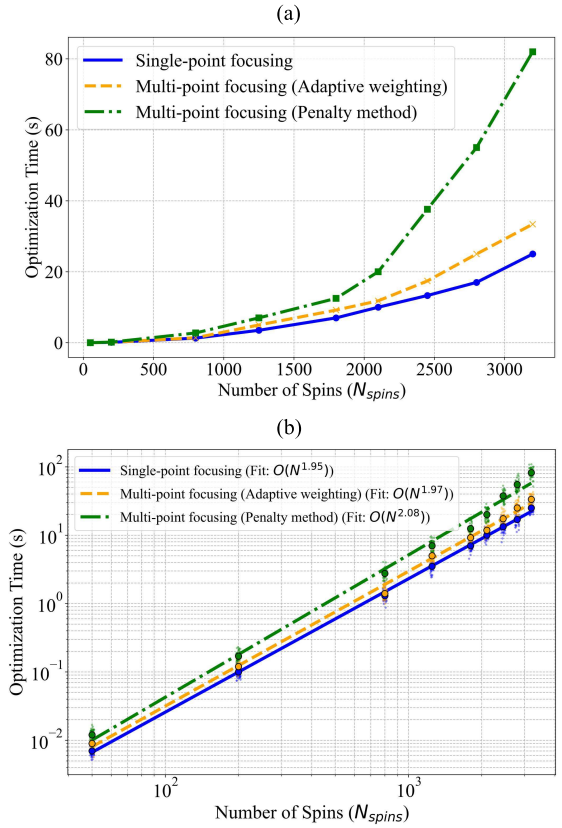

Fig. 7. Solving time of the dSB algorithm for different focusing scenarios. This figure presents a comprehensive view of the dSB algorithm's scalability. (a) Raw optimization time (in seconds) as a function of the total spin number (N_{spins}) on a linear scale. (b) Single-point focusing exhibits an approximate $O(N^{1.95})$ scaling, adaptive weighting multipoint focusing shows $O(N^{1.97})$ scaling, and the penalty method demonstrates $O(N^{2.08})$ scaling.

an approximate $O(N^{1.95})$ scaling, adaptive weighting multipoint focusing shows $O(N^{1.97})$ scaling, and the penalty method demonstrates $O(N^{2.08})$ scaling. This analysis corroborates the $O(N^2)$ scaling discussed in Section III-A, confirming the computational scalability of the dSB algorithm, which makes it highly applicable to our near-field metasurface problems. Although the algorithm imposes no fundamental limit on problem size, practical constraints such as computation time and memory usage become increasingly relevant as the number of spins grows. To further address these challenges, future work will explore strategies such as GPU acceleration and parallel computing, which hold promise for significantly reducing optimization time for ultralarge-scale designs.

IV. Numerical Results and Discussion

A. Benchmarking and Parameter Setting

1) Benchmarking Methods: To validate the efficiency and superiority of our dSB optimization algorithm, we benchmark its performance against several widely adopted conventional methods for metasurface phase optimization. These include the analytical PG method, and two widely-used stochastic optimization algorithms: SA and GA.

a) PG method: This is a conventional analytical approach that compensates for the propagation phase difference from each metasurface element to the target focal position to achieve coherent superposition. It provides a direct, noniterative solution based on geometric optics approximations. For a desired focal point (x_f, y_f, z_f), the required phase $\Phi(x_n, y_n)$ at each element (x_n, y_n) is typically given by

$$\Phi(x_n, y_n) = -k\sqrt{(x_n - x_f)^2 + (y_n - y_f)^2 + z_f^2}. \quad (20)$$

Physically, this formula dictates that the phase applied by each metasurface element must precisely compensate for the phase accumulated by a wave propagating from that element to the focal point, ensuring all waves arrive at the focal point in phase and constructively interfere, essentially creating a spherical wavefront converging to the target focus. While computationally efficient, this method is fundamentally constrained to simple focusing scenarios and often suffers from performance degradation due to inherent geometric approximations and phase quantization errors, particularly in the near-field where strong evanescent waves are present.

b) Simulated Annealing: SA is a metaheuristic algorithm inspired by the annealing process in metallurgy. It explores the solution space through stochastic state transitions, which are controlled by a gradually decreasing "temperature" parameter. This probabilistic search mechanism allows SA to escape local optima. In our benchmark, SA was configured with an initial temperature $T_0 = 1000$ K, an adaptive geometric cooling schedule (with a cooling rate $\alpha = 0.95$), and a Markov chain length $L = 100$. A maximum of 10^4 iterations was set. Conventional stochastic optimizers like SA can sometimes demonstrate significant efficiency-intensity tradeoffs, struggling to consistently achieve high-quality solutions within practical computational limits.

c) Genetic Algorithm: GA is an evolutionary optimization algorithm inspired by natural selection. It evolves a population of phase configurations through biological-inspired operations, including selection, crossover, and mutation, iteratively improving the population's fitness. For benchmarking, our GA implementation utilized 100 generations with a mutation rate (p_m) of 0.15 and a tournament selection size of 5. For the scale of problems considered (e.g., involving more than 480 binary variables for certain configurations), GA often fails to converge within reasonable computation times (e.g., within a 12-h computation limit), frequently generating suboptimal solutions with significant energy leakage.

2) Evaluation Metrics: To thoroughly evaluate the optimization results, we employ a comprehensive set of metrics that quantify both the quality of the achieved near-field focusing and the computational efficiency of the algorithms.

a) Quality Metrics: These metrics assess the physical characteristics and performance fidelity of the generated near-field patterns.

1) *Focusing Efficiency (η_{fc}):* Measures the proportion of the electric field intensity concentrated within the designated focal region (A_{fc}) on the observation plane, relative to the total input power (P_{in}). It is calculated as

$$\eta_{\text{fc}} = \frac{\iint_{A_{\text{fc}}} |\mathbf{E}(\mathbf{r})|^2 dS}{P_{\text{in}}} \quad (21)$$

where $\mathbf{E}(\mathbf{r})$ is the electric field vector at position $\mathbf{r}$ on the observation plane, dS is an infinitesimal area element,

and the integral is performed over the defined focal area A_{fc}. A higher η_{fc} indicates a more effective energy concentration.

2) *Focal Spot Size:* Quantifies the sharpness and resolution of the focal spot. For a single focal point, it is typically measured as the full width at half maximum (FWHM) of the intensity profile along the principal axes (e.g., x-, y-, and z-directions) within the focal plane. FWHM is determined by the lateral distance over which the intensity drops to half of its peak value. A smaller FWHM indicates a tighter and higher resolution focal spot.

3) *Multipoint Focusing Energy Uniformity:* Evaluates the balance of energy distribution among multiple focal points. For K target focal points with individual peak intensities $I_1, I_2, \ldots, I_K$, uniformity is quantified by the standard deviation of these intensities, normalized by their mean to provide a relative measure

$$\text{Uniformity} = \frac{\text{std}(I_1, I_2, \ldots, I_K)}{\text{mean}(I_1, I_2, \ldots, I_K)}. \tag{22}$$

A lower uniformity value (approaching zero) indicates a more balanced and even energy distribution among the target focal points.

b) Efficiency metrics: These metrics evaluate the computational performance and reliability of the optimization algorithms.

1) *Single-Run Time (t_s):* Represents the average computational time required for a single, complete execution of an algorithm to yield a solution. This value is obtained by averaging the measured execution time over multiple independent runs.

2) *Time-to-Target (TTT):* TTT is a key metric for evaluating the practical efficiency and reliability of optimization algorithms. It quantifies the expected computation time required for an algorithm to reach a predefined target solution quality with a specified confidence level. It is calculated as

$$\text{TTT} = \frac{\ln(1 - P_d)}{\ln(1 - P_s)} \times t_s \tag{23}$$

where P_d is the desired success probability (set to 99% for high reliability, i.e., $P_d = 0.99$), and P_s is the success probability of finding the target solution in a single run. The definition of the "target solution" (i.e., the specific quality threshold that determines P_s) is based on the particular focusing performance goals for each problem, such as achieving a certain focusing efficiency or a uniformity threshold. To ensure statistical significance in estimating P_s and t_s, we conducted 1000 independent experiments for each algorithm and problem configuration.

B. Single-Point Focusing

Our first set of numerical results focuses on the fundamental task of single-point near-field focusing. The objective is to concentrate incident electromagnetic energy into a single, tightly confined focal spot. Specifically, we designed a 41×41 metasurface array (total $N_{\text{elements}} = 1681$) and aimed to achieve a focus at the target point (0, 0.15, and 0.6 m). For the single-point focusing case, the decay constant K is set to 0.5, and the evolving temperature is $p(t) = 0.01t$; the detuning frequency Δ is 1. The maximum number of optimization steps is set as 5. The key dynamic parameter ξ, which defines the threshold for state locking, was empirically tuned from 1e-8 to 1, ensuring optimal performance. Our approach involves a parallel parameter sweep to quickly identify the best parameter range before conducting a more detailed sweep [38].

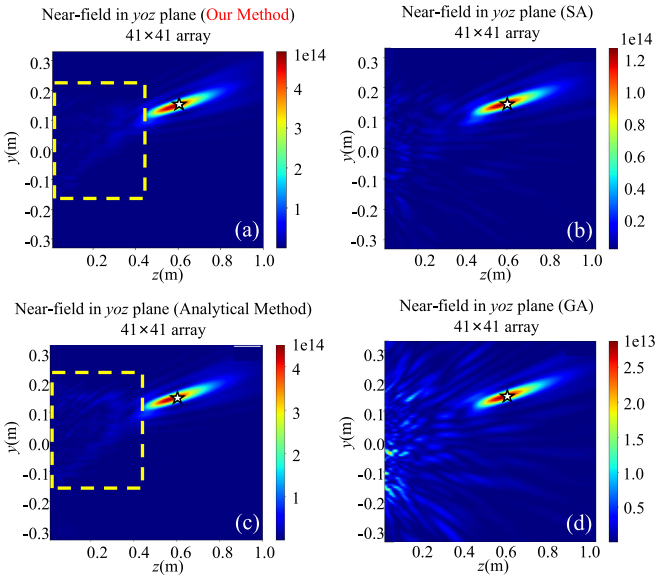

Fig. 8. Comparison of near-field focusing performance for single-point focusing. This figure visually compares the near-field intensity distributions at the focal plane (z = 0 m) obtained by different optimization methods. (a) dSB result: near-field power distribution optimized by the dSB algorithm, showing a tightly confined focus with suppressed energy leakage. (b) SA result: near-field power distribution optimized by the SA algorithm. (c) PG result: near-field power distribution obtained by the PG method. (d) GA result: near-field power distribution optimized by the GA.

The quantitative performance of dSB and the benchmark methods (PG, SA, and GA) is summarized in Table II. The resulting near-field power distributions generated by these four methods are visually compared in Fig. 8. These distributions were obtained from the best-performed runs after 1000 independent experiments on a single-core Intel[1] Core[2] i7-9700 processor and coding language Python.

As quantified in Table II and visually confirmed in Fig. 8, the dSB algorithm demonstrates superior performance in achieving high-quality single-point near-field focusing. For the TTT calculation, we set the target solution as achieving a focusing efficiency of 4.5% with a desired success probability (P_d) of 99%. dSB achieves the highest focusing efficiency of 9.17%, outperforming all benchmark methods with a robust "average focusing efficiency" of 8.70% over 1000 runs. Its focal spot is tight, with FWHM of 0.035 m in Y and 0.140 m in Z. Furthermore, dSB achieves this high performance with a competitive single-run computation time of 25.00 s and a remarkably low TTT of 25.00 s, indicating its high reliability in reaching the optimal solution.

[1]Registered trademark.
[2]Trademarked.

TABLE II
PERFORMANCE METRICS FOR SINGLE-POINT NEAR-FIELD FOCUSING

Method	Best Focusing Eff. (η_{fc}, %)	Avg. Focusing Eff. (η_{fc}, %)	FWHM (Y, m)	FWHM (Z, m)	Comp. Time (t_s, s)	TTT (s)
dSB	9.17	8.70	0.035	0.140	25.00	25.00
PG	8.79	8.79	0.036	0.140	0.001	N/A
SA	4.59	2.01	0.034	0.130	30.00	5456.84
GA	2.28	1.54	0.038	0.154	43980	N/A

In comparison, the PG method, while being the fastest with a single-run computation time of 0.001 s (as an analytical solution, TTT is not applicable), achieves a slightly lower "Best Focusing Efficiency" of 8.79% and a marginally larger focal spot (FWHM of 0.036 m in Y, 0.140 m in Z). Fig. 8(c) clearly shows that PG suffers from a slightly higher energy leakage (visible in the yellow-marked region) compared to dSB [Fig. 8(a)]. This is attributed to PG's inherent reliance on geometric optics approximations and susceptibility to quantization-induced errors, which are more pronounced in the nearfield.

Conventional stochastic optimizers, SA and GA, exhibit significant tradeoffs and limitations for this problem. SA shows a "Best Focusing Efficiency" of only 4.59% and a very low "Average Focusing Efficiency" of 2.01%. Although it achieves a tight FWHM (0.034 m in Y, 0.130 m in Z), its overall performance is significantly hampered by a high TTT of 5456.84 s, indicating poor reliability in reaching high-quality solutions. Fig. 8(b) visually confirms significant energy leakage. GA performs the worst, with a "Best Focusing Efficiency" of only 2.28% and an "Average Focusing Efficiency" of 1.54%. Its single-run computation time is extremely high (43 980 s), and it failed to reach the defined target solution reliably enough for TTT calculation. Fig. 8(d) clearly illustrates its suboptimal focusing with substantial energy leakage.

Our method consistently demonstrates effective focusing with low energy leakage. This superior performance is a direct result of the dSB algorithm's inherent advantage in exploring complex, high-dimensional energy landscapes and effectively escaping local optima. As the array size increases, the degrees of freedom of the optimization problem grow dramatically, making conventional stochastic algorithms like SA and GAs more susceptible to getting trapped in local optima.

In conclusion, for this fundamental single-point near-field focusing problem, the dSB algorithm consistently demonstrates superior efficiency and performance compared to both analytical and conventional stochastic optimization methods, offering a robust and reliable solution. It is noteworthy that although our dSB method can surpass the performance of the PG method in terms of achievable focusing quality, it is generally less efficient than PG when considering single-run time and average performance. Therefore, PG should be chosen when real-time modulation is a primary requirement, whereas dSB is the preferred choice when seeking the absolute best optimization results.

C. Multipoint Focusing

Beyond single-point focusing, the ability to generate multiple, simultaneous focal spots with desired characteristics is crucial for advanced near-field applications like multitarget sensing or parallel wireless power transfer. We present the performance of our dSB optimization framework for multipoint focusing, utilizing the adaptive weighting scheme and the penalty method, and compares our results with those obtained from the PG method for similar multipoint tasks. In these scenarios, in addition to the core dSB parameters (with $R_k = 1.0$, $K = 0.5$, $\Delta = 1.0$, and $p(t) = 0.01t$), the update interval Δt for the adaptive weights w_p is set to 5 based on empirical analysis, which provides a stable and efficient balance. The maximum number of optimization steps is set to 100. Similar to the single-point case, the parameter ξ was tuned to achieve the best solution quality.

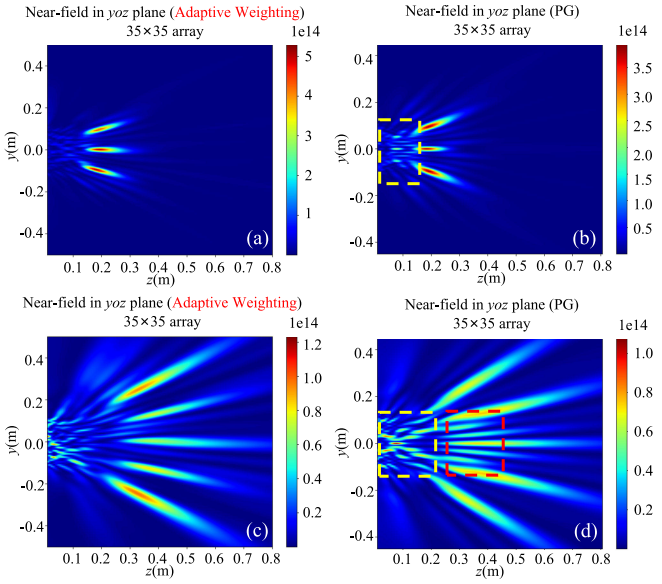

Fig. 9. Multipoint near-field focusing performance comparison. This figure presents the near-field intensity distributions at the focal plane (x-axis, specified in target coordinates) for two multipoint focusing scenarios, comparing dSB's adaptive weighting scheme with the PG method. (a) Three-point focusing (dSB adaptive weighting): Near-field intensity distribution for a 35×35 array generating three uniform focal points at (0, $\pm$0.1, and 0.2 m) and (0, 0, and 0.2 m). (b) Three-point focusing (PG method): near-field intensity distribution for the same three-point scenario, obtained using the PG method. (c) Five-point focusing (dSB adaptive weighting): near-field intensity distribution for a 35×35 array generating five uniform focal points at (0, 0.3, and 0.4 m), (0, 0.15, and 0.45 m), (0, 0, and 0.5 m), (0, $-$0.15, and 0.45 m), and (0, $-$0.3, and 0.4 m). (d) Five-point focusing (PG method): near-field intensity distribution for the same five-point scenario, obtained using the PG method.

1) yoz Plane Targets: Our investigation includes two distinct multipoint focusing examples where targets are located in the yoz plane, visually depicted in Fig. 9.

a) Three-point focusing [Fig. 9(a) and (b)]: We first consider a 35×35 metasurface array tasked with generating three

TABLE III
PERFORMANCE METRICS FOR MULTIPOINT NEAR-FIELD FOCUSING (35 × 35 METASURFACE)

Scenario	Total Eff. (η_{fc}, %)	Uniformity	Avg. FWHM (Y, m)	Avg. FWHM (Z, m)
3 points (dSB Adaptive)	18.421	0.0490	0.0475	0.2185
3 points (PG)	17.792	0.0223	0.0535	0.2210
5 points (dSB Adaptive)	39.478	0.2631	0.3117	0.5871
5 points (PG)	32.682	0.1154	0.4582	0.7539

focal points with 1:1:1 energy ratios. The target coordinates are (0, 0.1, and 0.2 m), (0, 0, and 0.2 m), and (0, −0.1, and 0.2 m). Fig. 9(a) shows the result obtained using our dSB algorithm with the adaptive weighting scheme, while Fig. 9(b) presents the corresponding result from the PG method.

For this three-point focusing example, our dSB adaptive weighting scheme achieves a total focusing efficiency of 18.421%, which is significantly higher than PG's 17.792% (as seen in Table III). While PG shows a numerically lower (better) uniformity of 0.0223 compared to dSB's 0.0490, it shows a worse average FWHM as seen in Table III. Furthermore, Fig. 9(b) critically reveals qualitative differences: distinct energy leakage is observed in regions between the focal spots and the array (the yellow box region) in the PG result. And the focal spots at (0, ±0.1, and 0.2 m) generated by the PG method appear noticeably larger and less focused than those achieved by our dSB method. This demonstrates that despite numerical advantages in specific metrics, dSB yields a qualitatively cleaner and more concentrated focus.

b) Five-point focusing [Fig. 9(c) and (d)]: Building on the complexity, we then explore a 35 × 35 metasurface array designed to generate five uniformly distributed focal points. The target coordinates are (0, 0.3, and 0.4 m), (0, 0.15, and 0.45 m), (0, 0, and 0.5 m), (0, −0.15, and 0.45 m), and (0, −0.3, and 0.4 m). Fig. 9(c) displays the result using our dSB algorithm with the adaptive weighting scheme, while Fig. 9(d) shows the PG method's result.

For this more complex five-point focusing example, our dSB adaptive weighting scheme achieves a total focusing efficiency of 39.478%, which is substantially higher than PG's 32.682% (as seen in Table III). Similar to the three-point case, PG exhibits numerically better uniformity (0.1154 versus dSB's 0.2631), but suffers from the FWHM size, which means it gains less focusing. However, Fig. 9(d) vividly illustrates the critical qualitative drawbacks of the PG method: it exhibits significantly higher energy leakage in the yellow box region compared to Fig. 9(c). More critically, pronounced energy leakage is also observed between adjacent focal points (the red box region), which could lead to significant interference and crosstalk in communication or sensing applications. In contrast, dSB [Fig. 9(c)] maintains a much cleaner field distribution with less interference, even with a numerically high uniformity metric in this specific instance.

To more intuitively demonstrate the performance advantages of our method, we further present the quantized phase distributions of both the dSB and PG methods for the two different multipoint focusing scenarios, as shown in Fig. 10. It is evident that our dSB method generates a complex and

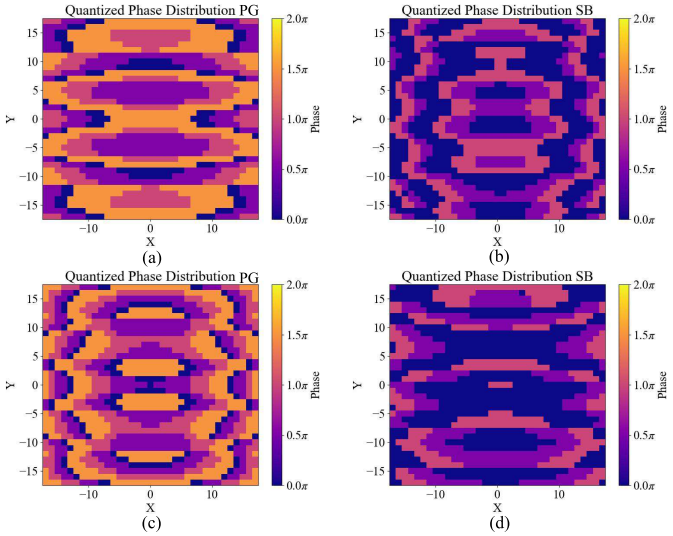

Fig. 10. Quantized phase distributions for the two multipoint focusing examples in (a) and (b) results for the three-point focusing scenario using the PG and dSB methods, respectively. (c) and (d) Results for the five-point focusing case.

irregular phase distribution [as shown in Fig. 10(b) and (d)], which is crucial for achieving precise control over multiple near-field targets. In contrast, the conventional PG method simply quantizes the phase to the nearest value, resulting in a relatively simple and linear phase distribution [as shown in Fig. 10(a) and (c)]. This unit-by-unit approximation, when applied across the entire metasurface, leads to significant performance degradation in complex scenarios. This notable difference in the phase distributions directly explains why our method achieves higher efficiency and cleaner focal spots.

2) xoy Plane Targets: We further demonstrate further demonstrates the versatility of our multiobjective optimization strategies by addressing multipoint focusing in the *xoy* plane (i.e., on a plane parallel to the metasurface, at a fixed z distance). This scenario is particularly relevant for applications like near-field display or optical manipulation. Fig. 11 visually presents the results for several complex multipoint focusing tasks.

a) Symmetric pattern uniform focusing [Fig. 11(a)–(c)]: We first investigate the generation of multiple uniform focal points on the *xoy* plane. Fig. 11(a) displays the result for an eight-point focus using a 20 × 20 array using the adaptive weighting scheme. The target coordinates are (±0.05, ±0.05, and 0.1 m), (0, ±0.05, and 0.1 m), and (±0.05, 0, and 0.1 m). Fig. 11(b) shows a four-point focusing result using the penalty method on a 20 × 20 array, with target points at (±0.025,

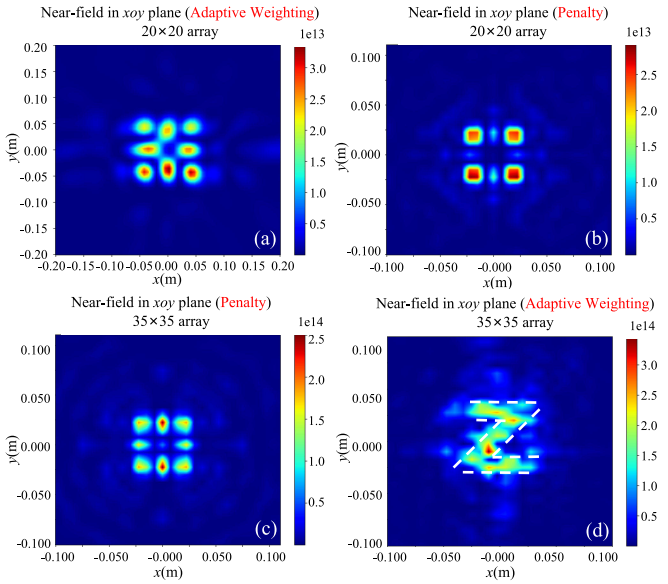

Fig. 11. Multipoint near-field focusing on the *xoy* plane. This figure illustrates the performance of dSB's multiobjective strategies for generating complex patterns on a plane parallel to the metasurface. (a) Eight-point uniform focusing (adaptive weighting, 20×20 array): near-field intensity distribution showing uniform focusing at eight points: (± 0.05, ± 0.05, and 0.1 m), (0, ± 0.05, and 0.1 m), (± 0.05, 0, and 0.1 m), using the adaptive weighting scheme. (b) Four-point uniform focusing (penalty method, 20×20 array): near-field intensity distribution showing uniform focusing at four points: (± 0.025, ± 0.025, and 0.15 m), using the penalty method. (c) Eight-point uniform focusing (penalty method, 35×35 array): near-field intensity distribution for the same eight target points as in (a), but on a larger 35×35 array, optimized using the penalty method. (d) Z-shape pattern generation (adaptive weighting, 35×35 array): near-field intensity distribution demonstrating the generation of a complex, asymmetric "Z-shape" pattern, achieved by pixelating the target shape into discrete focal points and optimizing with the adaptive weighting scheme.

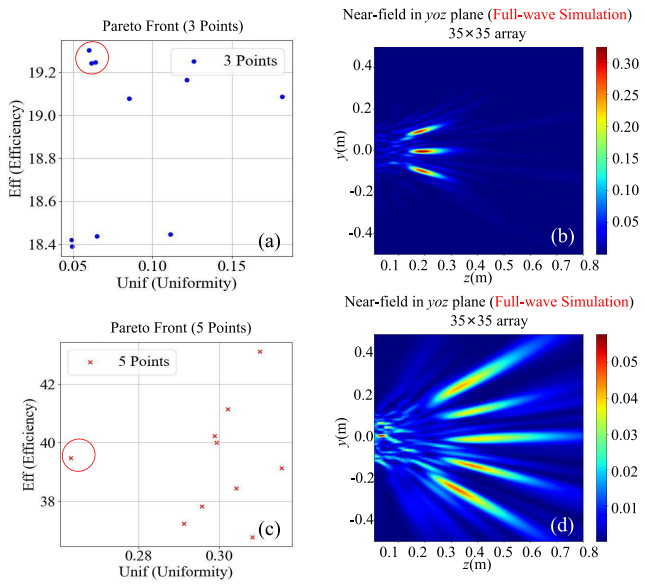

Fig. 12. Multiobjective performance tradeoff and full-wave validation. This figure illustrates the Pareto front exploration for multipoint focusing and validates selected solutions with full-wave simulations. (a) Pareto front for three-point focusing: scatter plot showing total efficiency versus uniformity from 100 random dSB runs, with the top 10% performing solutions (or specific Pareto-optimal points) highlighted. (b) HFSS simulation of selected three-point solution: full-wave near-field intensity distribution obtained from HFSS for a chosen solution from the Pareto front in (a). (c) Pareto front for five-point focusing: similar scatter plot for the five-point focusing scenario. (d) HFSS simulation of selected five-point solution: full-wave near-field intensity distribution from HFSS for a chosen solution from the Pareto front in (c).

± 0.025, and 0.15 m). Both the adaptive weighting and penalty methods can effectively achieve uniform focusing for such symmetric patterns. Quantitatively, the penalty method typically yields better uniformity in these scenarios.

For comparison, to demonstrate the capability for higher resolution and more complex patterns, we consider an eight-point focusing task [same target points as in Fig. 11(a)] but on a larger 35×35 array using the penalty method. Fig. 11(c) illustrates this result. Comparing it with Fig. 11(a), the larger array size significantly improves the resolution, leading to smaller and sharper focal spots. Furthermore, the penalty method generally achieves better uniformity for these symmetric patterns. However, a significant limitation of the penalty method is that it primarily finds solutions for symmetric target patterns and exhibits a lower success probability for more complex or asymmetric configurations.

b) Asymmetric Pattern Generation [Fig. 11(d)]: Consequently, for generating asymmetric or highly intricate near-field patterns, the adaptive weighting scheme becomes indispensable. Fig. 11(d) showcases the generation of a complex, asymmetric "Z-shape" pattern, which cannot be reliably achieved by the penalty method. To create such a pattern, we pixelate the target shape into discrete focal points based on the system's spatial resolution. The approximate resolution of the focusing system, determining the minimum achievable spot size, can be estimated by testing the FWHM of a typical single focal spot generated by this metasurface configuration. By setting the target points at intervals corresponding to this resolution, the adaptive weighting method effectively reconstructs the desired asymmetric pattern, demonstrating its robustness for complex pattern generation.

D. Multiobjective Tradeoff and Full-Wave Verification

In multiobjective optimization, especially for complex metasurface designs, simply achieving optimal performance for individual metrics is often insufficient. As previously analyzed in Section III-B2 regarding weight sensitivity, multiobjective problems inherently involve various tradeoffs, most commonly between total focusing efficiency and the uniformity among target points. Furthermore, practical applications may demand specific attention to additional performance indicators. Therefore, the ability to identify the Pareto front and select a suitable solution based on specific problem requirements is paramount. Our solver's inherent parallelism and efficient parameter tuning capabilities allow us to swiftly explore the performance landscape and construct the Pareto front from numerous optimization runs.

To demonstrate this, we conduct an analysis of the Pareto set for the two *yoz* plane multipoint focusing examples previously presented in Section IV-C1 (three-point and five-point focusing). For each scenario, we performed 100 random parameter tunings (e.g., varying initial conditions and parameters) and analyzed their best-performing results.

Fig. 12(a) and (c) illustrates the Pareto fronts obtained for the three-point and five-point focusing scenarios, respec-

tively, showing the tradeoff between total focusing efficiency and uniformity across the top ten best-performing examples. Among them, the solutions marked with red circles effectively balance competing objectives. Our ability to efficiently identify and explore these Pareto-optimal solutions allows designers to choose the optimal tradeoff point based on specific application requirements.

To validate the robustness of our method and the fidelity of the obtained solutions, the selected candidate cases from the Pareto fronts were subjected to full-wave electromagnetic simulations using HFSS. The resulting near-field energy distributions are presented in Fig. 12(b) for the three-point case and Fig. 12(d) for the five-point case. There are indeed some discrepancies between our theoretical optimization results and the full-wave simulation results. These differences are precisely caused by nonideal factors, such as the mutual coupling between units and the influence of the feed network. Nevertheless, our method consistently demonstrates effective multipoint focusing with low energy leakage. The ability to efficiently construct the Pareto front and select physically validated solutions offers a powerful solution framework for designing complex multiobjective near-field metasurfaces.

V. Conclusion

In conclusion, we have presented a robust quantum-inspired optimization framework for near-field metasurface design. A key contribution of our work is the pioneering application of the dSB algorithm to solve complex multiobjective problems. To tackle the inherent tradeoffs in multiobjective designs, we introduced two novel strategies: an adaptive weighting scheme for achieving arbitrary intensity ratios and a penalty method for enforcing energy uniformity. This framework is not limited to a specific unit-cell type or quantization level; instead, it is designed to map any unit-cell's complex response to a binary spin representation, making it applicable to different metasurface architectures and multibit quantization schemes. We also rigorously validated these designs through full-wave simulations. Compared to previous works, our method offers unique advantages in both algorithmic efficiency and framework design, ensuring scalability for large-scale problems and providing a robust approach for finding reliable, high-quality solutions.

Our contributions significantly advance metasurface design. In summary, our dSB optimization framework offers a versatile and efficient set of solutions tailored to different focusing requirements.

1) *For Single-Point Focusing Tasks:* If a fast solution is needed, the PG method should be chosen; if superior focusing performance is desired, our dSB algorithm is the preferred choice.
2) *In Multipoint Focusing Scenarios:* When generating simple, symmetric patterns with a stringent requirement for energy uniformity, the penalty method proves highly effective; whereas for more complex, asymmetric patterns or when precise control over arbitrary energy ratios is needed, the adaptive weighting scheme is indispensable.

Furthermore, our solver can output multiple optimization results and supports selection on the Pareto front, thereby providing designers with optimal performance tradeoffs. This study's core innovation lies in our pioneering exploration of the quantum-inspired algorithm in near-field electromagnetic problems, and we demonstrate its superior performance over conventional stochastic optimization methods in efficiency, focusing quality, and reliability over conventional stochastic optimization methods. Our comprehensive weight sensitivity analysis provides a versatile framework for navigating complex performance tradeoffs. The scalability analysis confirms a favorable polynomial complexity of $O(N_{\text{spins}}^2)$ across all scenarios, proving the framework's practicality and enabling the construction and selection of physically validated solutions from the Pareto front.

Despite the power of the proposed dSB optimization framework, it does have certain limitations and tradeoffs. Compared to analytical methods, dSB is an iterative algorithm that requires more computation time to find the optimal solution. This creates a clear tradeoff between computational efficiency and final performance. Furthermore, the Green's function model used for optimization is a simplification of the real electromagnetic environment, which may limit the theoretical optimality of the solutions. Looking forward, our research will explore pushing the boundaries of computational efficiency through massive GPU acceleration and parallel computing strategies. We also aim to address model-simulation discrepancies by incorporating more detailed coupling effects and nonideal element characteristics into the optimization model, alongside experimental validation of these complex near-field designs. Further expansion of the framework's capabilities to dynamically reconfigurable metasurfaces and even more sophisticated arbitrary field shaping will be pursued.

References

[1] H.-T. Chen, A. J. Taylor, and N. Yu, "A review of metasurfaces: Physics and applications," *Rep. Prog. Phys.*, vol. 79, no. 7, Jul. 2016, Art. no. 076401.
[2] D. Lin, P. Fan, E. Hasman, and M. L. Brongersma, "Dielectric gradient metasurface optical elements," *Science*, vol. 345, no. 6194, pp. 298–302, Jul. 2014.
[3] H.-H. Hsiao, C. H. Chu, and D. P. Tsai, "Fundamentals and applications of metasurfaces," *Small Methods*, vol. 1, no. 4, Apr. 2017, Art. no. 1600064.
[4] S.-Q. Li, X. Xu, R. Maruthiyodan Veetil, V. Valuckas, R. Paniagua-Domínguez, and A. I. Kuznetsov, "Phase-only transmissive spatial light modulator based on tunable dielectric metasurface," *Science*, vol. 364, no. 6445, pp. 1087–1090, Jun. 2019.
[5] S. Yu, D. Guan, Z. Gu, J. Shi, Z. Liu, and Y. Liu, "Phase-only beam forming method based on digital code metasurface," *IEEE Trans. Aerosp. Electron. Syst.*, vol. 61, no. 1, pp. 121–134, Feb. 2025.
[6] S. Zhuo et al., "Dynamic transmissive metasurface for broadband phase-only modulation based on phase-change materials," *Laser Photon. Rev.*, vol. 17, no. 1, Jan. 2023, Art. no. 2200403.
[7] Y. Wang, C. Pang, Q. Wang, Y. Mu, Y. Cheng, and J. Qi, "Phase-only compact radiation-type metasurfaces for customized far-field manipulation," *IEEE Trans. Microw. Theory Techn.*, vol. 71, no. 9, pp. 4119–4128, Sep. 2023.
[8] A. Li, S. Singh, and D. Sievenpiper, "Metasurfaces and their applications," *Nanophotonics*, vol. 7, no. 6, pp. 989–1011, 2018.
[9] J. Hu, S. Bandyopadhyay, Y.-H. Liu, and L.-Y. Shao, "A review on metasurface: From principle to smart metadevices," *Frontiers Phys.*, vol. 8, Jan. 2021, Art. no. 586087.

[10] L. Huang, S. Zhang, and T. Zentgraf, "Metasurface holography: From fundamentals to applications," *Nanophotonics*, vol. 7, no. 6, pp. 1169–1190, Jun. 2018.
[11] L. Li, P. Zhang, F. Cheng, M. Chang, and T. J. Cui, "An optically transparent near-field focusing metasurface," *IEEE Trans. Microw. Theory Techn.*, vol. 69, no. 4, pp. 2015–2027, Apr. 2021.
[12] H. Zhang, N. Shlezinger, F. Guidi, D. Dardari, M. F. Imani, and Y. C. Eldar, "Beam focusing for near-field multiuser MIMO communications," *IEEE Trans. Wireless Commun.*, vol. 21, no. 9, pp. 7476–7490, Sep. 2022.
[13] S. W. D. Lim et al., "Point singularity array with metasurfaces," *Nature Commun.*, vol. 14, no. 1, p. 3237, Jun. 2023.
[14] H. Zhang, N. Shlezinger, F. Guidi, D. Dardari, M. F. Imani, and Y. C. Eldar, "Beam focusing for multi-user MIMO communications with dynamic metasurface antennas," in *Proc. IEEE Int. Conf. Acoust. Speech Signal Process. (ICASSP)*, Jun. 2021, pp. 4780–4784.
[15] Q. Yang et al., "Beam focusing for near-field multi-user localization," *IEEE Trans. Veh. Technol.*, vol. 74, no. 8, pp. 12259–12273, Aug. 2025.
[16] X. Wu et al., "Multitarget wireless power transfer system strategy based on metasurface-holography multifocal beams," *IEEE Trans. Microw. Theory Techn.*, vol. 71, no. 8, pp. 3479–3489, Aug. 2023.
[17] A. Ishimaru, *Electromagnetic Wave Propagation, Radiation, and Scattering: From Fundamentals to Applications*. Hoboken, NJ, USA: Wiley, 2017.
[18] Z. Yu, T. Zhao, S. Yue, H. Li, and H. Zhang, "Quantification phase gradient near-field focusing metasurface for microwave wireless power transfer system," *IEEE Antennas Wireless Propag. Lett.*, vol. 23, no. 6, pp. 1944–1948, Jun. 2024.
[19] K. Singh, M. U. Afzal, and K. P. Esselle, "Designing efficient phase-gradient metasurfaces for near-field meta-steering systems," *IEEE Access*, vol. 9, pp. 109080–109093, 2021.
[20] S. Kirkpatrick, C. D. Gelatt, and M. P. Vecchi, "Optimization by simulated annealing," *Sci.*, vol. 220, no. 4598, pp. 671–680, 1983.
[21] S. Mirjalili, *Evolutionary Algorithms and Neural Networks*. New York, NY, USA: Springer, 2019.
[22] X. Y. Lu and Z. Q. Lu, "Numerical optimization for radiated noises of centrifugal pumps in the near-field and far-field based on a novel MLGA-PSO algorithm," *J. Vibroengineering*, vol. 19, no. 7, pp. 5589–5605, Nov. 2017.
[23] W. Liu, H. Ren, C. Pan, and J. Wang, "Deep learning based beam training for extremely large-scale massive MIMO in near-field domain," *IEEE Commun. Lett.*, vol. 27, no. 1, pp. 170–174, Jan. 2023.
[24] G. Jiang and C. Qi, "Near-field beam training based on deep learning for extremely large-scale MIMO," *IEEE Commun. Lett.*, vol. 27, no. 8, pp. 2063–2067, Aug. 2023.
[25] J. M. Arrazola, A. Delgado, B. R. Bardhan, and S. Lloyd, "Quantum-inspired algorithms in practice," *Quantum*, vol. 4, p. 307, Aug. 2020.
[26] G. Zhang, "Quantum-inspired evolutionary algorithms: A survey and empirical study," *J. Heuristics*, vol. 17, no. 3, pp. 303–351, Jun. 2011.
[27] J. D. Hidary, *Quantum Computing: An Applied Approach*, 2nd ed., Cham, Switzerland: Springer, 2021.
[28] J. E. Moyal, "Quantum mechanics as a statistical theory," *Math. Proc. Cambridge Phil. Soc.*, vol. 45, no. 1, pp. 99–124, 1949.
[29] Q.-G. Zeng, X.-P. Cui, B. Liu, Y. Wang, P. Mosharev, and M.-H. Yung, "Performance of quantum annealing inspired algorithms for combinatorial optimization problems," *Commun. Phys.*, vol. 7, no. 1, p. 249, Jul. 2024.
[30] E. Tang, "A quantum-inspired classical algorithm for recommendation systems," in *Proc. 51st Annu. ACM SIGACT Symp. Theory Comput.*, Jun. 2019, pp. 217–228.
[31] S. Yarkoni, E. Raponi, T. Bäck, and S. Schmitt, "Quantum annealing for industry applications: Introduction and review," *Rep. Prog. Phys.*, vol. 85, no. 10, Oct. 2022, Art. no. 104001.
[32] P. Hauke, H. G. Katzgraber, W. Lechner, H. Nishimori, and W. D. Oliver, "Perspectives of quantum annealing: Methods and implementations," *Rep. Prog. Phys.*, vol. 83, no. 5, May 2020, Art. no. 054401.
[33] H. Goto, "Bifurcation-based adiabatic quantum computation with a nonlinear oscillator network," *Sci. Rep.*, vol. 6, no. 1, p. 21686, Feb. 2016.
[34] H. Goto, K. Tatsumura, and A. R. Dixon, "Combinatorial optimization by simulating adiabatic bifurcations in nonlinear Hamiltonian systems," *Sci. Adv.*, vol. 5, no. 4, p. 2372, Apr. 2019.
[35] H. Goto et al., "High-performance combinatorial optimization based on classical mechanics," *Sci. Adv.*, vol. 7, no. 6, p. 7953, Feb. 2021.
[36] N. P. de Leon et al., "Materials challenges and opportunities for quantum computing hardware," *Science*, vol. 372, no. 6539, p. 2823, Apr. 2021.
[37] R. D'Cunha, T. D. Crawford, M. Motta, and J. E. Rice, "Challenges in the use of quantum computing hardware-efficient ansätze in electronic structure theory," *J. Phys. Chem. A*, vol. 127, no. 15, pp. 3437–3448, 2023.
[38] Y. Jiang et al., "Quantum-inspired beamforming optimization for quantized phase-only massive MIMO arrays," 2024, *arXiv:2409.19938*.
[39] S. S. A. Yuan et al., "Quantum annealing-inspired optimization for space–time coding metasurface," *IEEE Trans. Antennas Propag.*, vol. 73, no. 9, pp. 6512–6524, Sep. 2025.
[40] Y. Jiang, S. S. A. Yuan, and W. E. I. Sha, "Near-field beamforming with quantum inspired optimization," in *IEEE MTT-S Int. Microw. Symp. Dig.*, China, May 2025, pp. 1–3.
[41] L. Tsang, J. A. Kong, and R. T. Shin, *Theory of Microwave Remote Sensing*. New York, NY, USA: Wiley-Blackwell, 1985.
[42] C. Ross, G. Gradoni, Q. J. Lim, and Z. Peng, "Engineering reflective metasurfaces with Ising Hamiltonian and quantum annealing," *IEEE Trans. Antennas Propag.*, vol. 70, no. 4, pp. 2841–2854, Apr. 2022.
[43] H. Obata, T. Nabetani, H. Goto, and K. Tatsumura, "Ultra-high-speed optimization for 5G wireless resource allocation by simulated bifurcation machine," in *Proc. IEEE Wireless Commun. Netw. Conf. (WCNC)*, Apr. 2024, pp. 1–6.
[44] G. F. Newell and E. W. Montroll, "On the theory of the Ising model of ferromagnetism," *Rev. Mod. Phys.*, vol. 25, no. 2, pp. 353–389, Apr. 1953.
[45] T. D. Schultz, D. C. Mattis, and E. H. Lieb, "Two-dimensional Ising model as a soluble problem of many fermions," *Rev. Mod. Phys.*, vol. 36, no. 3, pp. 856–871, Jul. 1964.
[46] F. Glover, G. Kochenberger, and Y. Du, "A tutorial on formulating and using QUBO models," 2018, *arXiv:1811.11538*.
[47] D. Pastorello and E. Blanzieri, "Quantum annealing learning search for solving QUBO problems," *Quantum Inf. Process.*, vol. 18, no. 10, p. 303, Oct. 2019.
[48] E. Boros and P. L. Hammer, "Pseudo-Boolean optimization," *Discrete Appl. Math.*, vol. 123, nos. 1–3, pp. 155–225, Nov. 2002.
[49] S. Jiang, K. A. Britt, A. J. McCaskey, T. S. Humble, and S. Kais, "Quantum annealing for prime factorization," *Sci. Rep.*, vol. 8, no. 1, p. 17667, Dec. 2018.
[50] K. Mato, R. Mengoni, D. Ottaviani, and G. Palermo, "Quantum molecular unfolding," *Quantum Sci. Technol.*, vol. 7, no. 3, Jul. 2022, Art. no. 035020.
[51] T. Kanao and H. Goto, "Simulated bifurcation for higher-order cost functions," *Appl. Phys. Exp.*, vol. 16, no. 1, Jan. 2023, Art. no. 014501.